Using a broadband long-wavelength channel to increase the capture range of segment piston phase retrieval for segmented-aperture systems

JOSEPH S. H. TANG* AND JAMES R. FIENUP

Institute of Optics, University of Rochester, 480 Intercampus Drive, Rochester, New York 14627, USA
*jtang19ur@gmail.com

Segmented-aperture systems, such as the James Webb Space Telescope (JWST), require fine piston alignment between primary mirror segments. Computer simulation experiments show that using a broadband long-wavelength channel, illustrated with the Mid Infrared Instrument (MIRI) onboard the JWST, can extend the capture range of segment piston phase retrieval significantly (in the case of JWST with MIRI, up to hundreds of microns), greatly reducing the requirements on coarse phasing.   © 2024 Optica Publishing Group

1. INTRODUCTION

Segmented-aperture systems provide a method of having a large primary collecting aperture without requiring a large monolithic aperture. However, one of the challenges of reflective segmented-aperture systems is segment piston alignment. Our work is motivated by the James Webb Space Telescope (JWST), which is a segmented-aperture system with a primary mirror that consists of 18 hexagonal segments in a two-ring configuration. To achieve the goal of JWST being diffraction-limited [1], the relative piston errors between segments needs to be less than 1/14 waves rms according to the Maréchal criterion. However, measurement error should be several times more stringent than the specification error in order to have high confidence that the telescope meets specification. Thus, we chose a measurement error of 1/100 waves as the criterion for measurement success. For the JWST, for which most of the wavefront sensing was done with the short-wavelength channel Near Infrared Camera (NIRCam) at a central wavelength of 2.12 µm, this corresponds to 21 nm.

To achieve such fine alignment, the JWST went through a multi-step wavefront sensing and control commissioning process [1,2]. Of particular interest to this paper is the fine phasing step, which uses phase retrieval to measure small phasing errors between segments, focusing on tip, tilt, and piston terms. Before the fine phasing step, there is an image stacking step and a coarse phasing step. The image stacking step corrects for large tip/tilt segment errors, and the coarse phasing step uses dispersed fringe sensing to correct for large piston errors (up to 350 µm) between segments. While coarse phasing can measure much larger segment piston errors than fine phasing, coarse phasing has residual errors that are too large for the fine alignment required for JWST. Thus, fine phasing is used to correct for residual segment piston errors from coarse phasing, as well as any residual tip/tilt from image stacking. The work in this paper aims to increase the magnitude of segment piston errors that the fine phasing step can measure while still meeting the required measurement error criterion.

Phase retrieval entails simulating a point spread function (PSF), an image of an unresolved star, from a phase estimate, then updating the phase estimate to minimize the error between the simulated PSF and the measured PSF [3]. Phase retrieval can be used to correct for multiple types of phase errors. In this paper, however, we will focus specifically on phase retrieval for segment piston error, because phase retrieval for segment piston errors of multiple wavelengths requires additional steps not used in regular phase retrieval. For brevity, we will use the term segment piston phase retrieval (SPPR) to refer to phase retrieval of only segment piston errors, which builds upon previous work done by Paine and Fienup [4]. In addition, we mainly explored the case where the segments are perfectly flat. While in reality this is not the case, intra-segment errors would be known from prior measurements (ground testing and phase retrieval on individual segments, as was done with JWST) and can be easily added to the forward model. Since intra-segment errors can be treated as prior knowledge and are not parameters to be solved for, unlike segment piston, their inclusion in the forward model would only somewhat affect the results of SPPR. We did examine a case where we included intra-segment error and system aberrations, which we describe more fully in Section 8.

A common issue in phase retrieval is the capture range problem. Phase retrieval can be cast as a nonlinear optimization problem [3], and the optimization process can get stuck (stagnate) in local minima that are not the true solution. The capture range is defined as the set of starting estimates that converge

to the true solution; conversely, starting estimates outside the capture range converge to other local minima. Increasing the capture range is directly correlated to improving the success rate, since increasing the capture range makes it more likely that the initial starting estimate will be within the capture range.

PSFs fundamentally depend on phase error, ϕ, rather than the optical path error, Δl, though the two are closely related by

$$\phi(x, y) = \frac{2\pi}{\lambda} \Delta l(x, y), \tag{1}$$

where λ is the wavelength in the monochromatic case, or the central wavelength in the narrowband case. In other words, for the same Δl, the resulting PSF will depend on the wavelength. Thus, the capture range for phase retrieval is more directly phase dependent than optical-path dependent. Therefore, the capture range in terms of optical path can be increased by using a longer wavelength, since longer wavelengths have smaller phase errors than shorter wavelengths for the same optical path error.

SPPR has two additional issues that make the problem of SPPR particularly difficult: piston ambiguity and deep local minima. Piston ambiguity is the problem where, for monochromatic light, a segment piston error of 2π gives the same PSF as zero error. The piston ambiguity problem can be solved by using broadband light, as described in Section 2. "Deep local minima" is the problem where it is difficult for a nonlinear optimization to get out of the local minimum it is currently in. The deep local minima problem associated with multiple-2π phases can be solved with a grid search, as described in Section 3. Previous work done by Paine showed that using broadband light with a grid search could greatly increase the capture range of SPPR [4]. Note that both broadband light and grid searching are needed to increase the capture range of SPPR: a grid search with monochromatic light has piston ambiguity, whereas the error metric for piston errors with broadband light has deep local minima.

Thus, in this paper, we explored using a broadband long-wavelength channel, specifically the F1800W broadband filter on the Mid Infrared Instrument (MIRI) onboard JWST, to increase the capture range of SPPR in terms of optical path error as compared with using NIRCam. We compared MIRI's F1800W broadband filter, which has a central wavelength of 18.06 µm, to NIRCam's F212N narrowband filter, which has a central wavelength of 2.12 µm. The ratio of central wavelengths between the MIRI F1800W and NIRCam F212N filters means that using MIRI can potentially increase the capture range by a factor of 8.5. In addition, using a broadband filter could increase the capture range over using a narrowband filter up to the coherence length of the spectrum, as described in Section 2. However, there is a trade-off in choice of bandwidth. Smaller bandwidths potentially have larger capture ranges since the coherence length is longer, but are more prone to the piston ambiguity problem. Conversely, larger bandwidths better deal with the piston ambiguity problem, but at the cost of smaller capture ranges. Since MIRI's F1800W broadband filter has a coherence length of approximately 6 waves at the 18.06 µm center wavelength, altogether the capture range can potentially be increased by a factor of 51. One additional benefit of using a broadband filter is if the telescope happened to be forced to use short exposures (e.g., if the telescope were to have jitter), where

the broadband PSF would have a few times more photons than with the narrowband filter.

While the capture range may increase with the longer wavelength, this comes at the cost of accuracy: the measurement accuracy of SPPR with MIRI relative to NIRCam will decrease by the same factor of 8.5. However, this can be satisfactory so long as the residual errors of phase retrieval with MIRI is less than the 21 nm goal. Alternatively, it can be adequate for the residual errors in phase retrieval with MIRI to be within the capture range of phase retrieval with NIRCam. In that case, an SPPR with MIRI followed by an SPPR with NIRCam can have the capture range of MIRI with the accuracy of NIRCam.

While our work follows closely to the work done by Paine and Fienup [4], there are key differences. First, the cases Paine analyzed were all broadband spectra that were symmetric, such as the one shown in Fig. 1(c), while our spectrum, which is based on 5700 K blackbody radiation going through MIRI's F1800W filter as shown in Fig. 1(e), is asymmetric. Having an asymmetric broadband spectrum creates a phase-shift problem in the grid search that requires an additional optimization step to the grid search to compensate, which we describe in Section 3. Paine did not have this additional optimization step because he would not have encountered this phase-shift problem with symmetric broadband spectra, which we explain in Section 3. Second, Paine uses three defocus planes, while we only use one defocus plane. Paine's work was more tailored towards using NIRCam, which is outfitted with a filter wheel with weak lenses that readily allow it to take images at three defocus planes. However, MIRI has no weak lenses and is only able to readily take images at one defocus plane, so we only used one defocus plane instead of three to reflect this. Both of these differences make SPPR more difficult with data from MIRI; nevertheless, using the longer wavelengths of MIRI greatly expands the capture range in terms of optical path error that can be accurately determined.

In this paper, we demonstrate that SPPR can estimate piston errors with reasonable success rates up to a few waves of MIRI's F1800W filter's center wavelength. This would greatly reduce the residual error requirements of the coarse phasing step, if not remove the need for dispersed fringe sensing altogether.

2. USING BROADBAND LIGHT TO SOLVE THE PISTON AMBIGUITY PROBLEM

One of the known problems of SPPR is that with a monochromatic light spectrum, the piston value of a single segment is ambiguous. This can be seen in Fig. 1(b), which shows the error metric value as a function of single-segment piston for a monochromatic spectrum. For the error metric, we used the bias-and-gain-invariant error metric as described by Thurman [5], which is a common error metric used in phase retrieval. The bias-and-gain-invariant error metric can be expressed as

$$E = \sum_{m, n} (\boldsymbol{D}[m, n] - \beta - \alpha \boldsymbol{I}[m, n])^2, \tag{2}$$

where $\boldsymbol{D}$ is the measured PSF, $\boldsymbol{I}$ is the simulated PSF, and α, β are estimated gain and bias terms, respectively. The aperture used was a JWST-like aperture, as shown in Fig. 2. The segments were assumed perfect (aside from piston errors), and no measurement noise was added to the measured PSF. From Fig. 1(b),
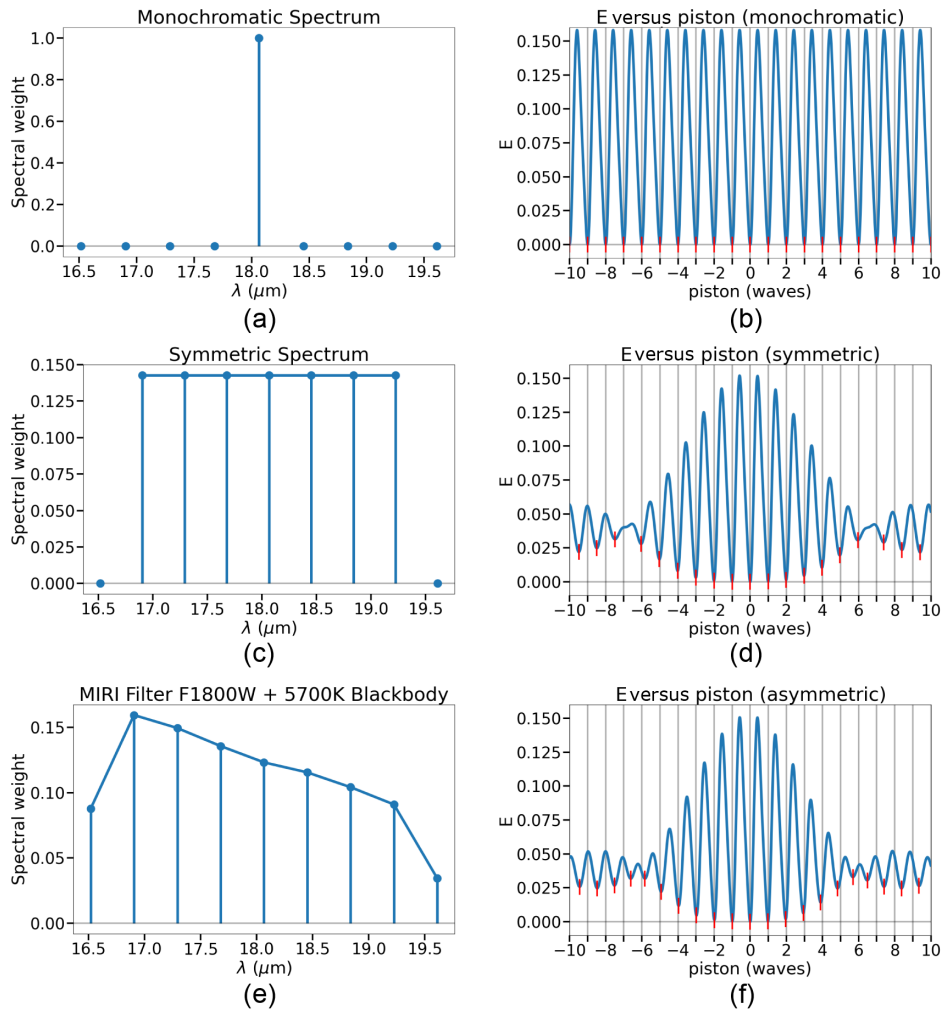
Fig. 1. Error metric value, E, versus single-segment piston for various spectra. Each row shows a spectrum on the left and its corresponding E versus single-segment piston on the right. The rows top to bottom correspond to monochromatic, symmetric broadband, and asymmetric broadband spectra. For the plots in the right column, the gray vertical lines are located at integer waves (in terms of the center wavelength) of piston, and the red vertical bars show the location of error metric troughs.
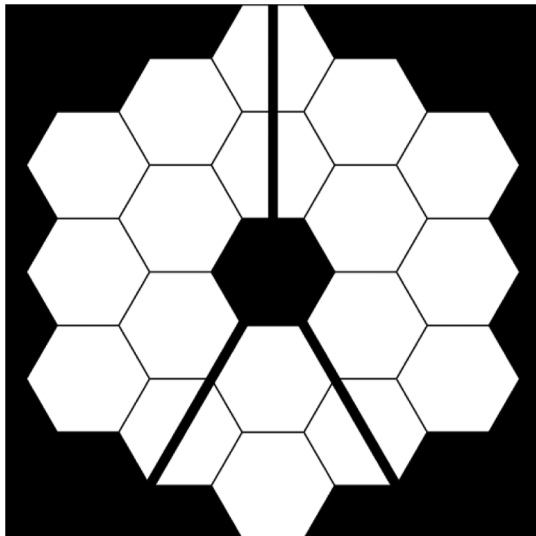

Fig. 2. JWST-like aperture.

we see that the error metric value as a function of a single-segment piston for a monochromatic spectrum is a sinusoid with a period of 1 wave, and that the error metric value is equivalently zero at every trough. This occurs because piston phase jumps of an integer times 2π on any segment represents the same complex-valued field in the pupil, that complex pupil generates the same PSF, and thus the error metric value would be the same for those cases. Thus, cases that differ by an integer times 2π piston errors on segments are indistinguishable according to the error metric, and therefore the solution is ambiguous. This demonstrates the piston ambiguity problem, because the true piston value is ambiguous with the piston values at all the other troughs in the error metric. This limits the capture range of SPPR for monochromatic light to each segment being within $\pm 1/2$ wave from a reference segment, since there is no guarantee that the retrieved solution is the true solution outside that range.

A solution to the integer-wavelength piston ambiguity problem is to use a polychromatic (broadband) light spectrum [4] rather than the usual near-monochromatic, narrowband light spectrum to define the optical bandwidth of the PSFs.

Generating broadband PSFs has some nuances that we detail in Section 4. Figure 1(d) shows the error metric as a function of a single-segment piston for a symmetric broadband spectrum. Single-segment 2π piston phase jumps (in terms of center wavelength) are now distinguishable (i.e., error metric value is different), since the broadband PSF now changes with multiple-2π phase jumps, whereas it did not in the monochromatic PSF case. This is due to how the PSF changes with wavelength. The PSF is a function of phase error, and phase error is a function of wavelength according to Eq. (1). In addition, the Fourier kernel in Fresnel propagation depends on the wavelength, which changes the magnification of the PSF. Thus, for a broadband PSF, fringe visibility in the PSF is reduced, since the PSF at one wavelength partially fills in the nulls of the PSF at another wavelength. More importantly, however, is that fringe visibility changes with multiple-2π phase jumps in the broadband PSF case and not in the monochromatic PSF case.

The coherence length describes the minimum segment piston separation between two segments for which light from the two segments has greatly diminished interference fringes, and the coherence length is inversely proportional to the bandwidth. In addition, for pure segment piston error, while at the focus plane the light from each segment overlaps one another, at a defocus plane the light from each segment starts to separate and overlap less. In order for a segment piston value to be retrievable, the light from that segment has to coherently interfere with light from at least one other segment in order for the PSF to vary with that segment piston value. Thus, the light from that segment must be within a coherence length difference in piston from another segment, and the overlap of light from the two segments needs to be sufficient to have discernible fringes. If the segment piston value is not within the coherence length of another segment or the overlap is insufficient, then the light from that segment will add incoherently to the PSF, and thus the PSF will not vary with that segment piston value; in this case, all we can determine is that the segment is outside the coherence length with any significant overlap of any other segments.

In the monochromatic case, the capture range is limited by piston ambiguity; thus the capture range of SPPR in the monochromatic case is limited to each segment being within $\pm 1/2$ wave from a reference segment. In the broadband case, the capture range is limited both by piston ambiguity and by the coherence length of the light with a given spectrum. If the bandwidth is too narrow, then the capture range can still be limited by piston ambiguity, but if the bandwidth is too wide, then the coherence length may be too short and again limit the capture range. Assuming that the bandwidth is chosen properly, then the capture range of SPPR in the broadband case is that each segment has to be within the coherence length with significant light overlap of at least one other segment, which may be significantly larger than the capture range in the monochromatic case. However, these are theoretical maxima of the capture range; the capture range can still be limited by other local minima.

3. USING GRID SEARCH TO SOLVE THE DEEP LOCAL MINIMA PROBLEM

While using a broadband spectrum makes single-segment 2π piston phase jumps distinguishable from one another, these
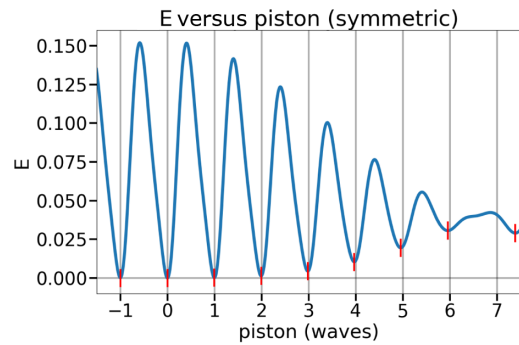

Fig. 3. Zoomed in plot of Fig. 1(d). For the symmetric spectrum case, the troughs land approximately on integer waves of piston error within the coherence length of ~ 6 waves.

solutions are still deep local minima (i.e., difficult to get out of) in the error metric landscape. This makes the grid search step in SPPR essential.

In previous work [4], Paine examined the case where the broadband spectrum was symmetric. Figure 1(d) shows an error metric value as a function of a single-segment piston for this symmetric-spectrum case. Figure 3 shows a zoomed in version of Fig. 1(d) in order to see the troughs better. Since the spectrum is broadband, the troughs have different error metric values, with the true piston value giving the lowest error, as previously discussed. Note that the bottoms of the troughs are approximately 1 wave (in terms of center wavelength) apart, as seen in Figs. 1(d) and 3. Since we know that these solutions are approximately single-segment integer waves (in terms of center wavelength) of piston phase jumps apart, we could try to perform a brute-force grid search that checks them all and choose the best one, i.e., evaluate the error metric for these solutions and select the one with the lowest error. However, there may be many possible 2π piston phase jumps per segment, and the combinatorics scales exponentially with the number of segments if we had to check every combination of segment piston phase jumps. For example, checking all combinations of just five piston phases for 17 segments requires $5^{17} = 30 \times 10^9$ cases. Instead, we perform a computationally faster grid search that limits the number of phase jumps to test by modifying one segment at a time, which is further detailed in Section 5.

For an asymmetric broadband spectrum, most of the intuition is the same as in the symmetric broadband case, but it is no longer valid to assume that the bottoms of the troughs are approximately 1 wave (in terms of center wavelength) apart. Instead, the bottoms of the troughs may have a phase shift. This can be seen in Fig. 4(a), especially at 4 and 5 waves of segment piston. Changing the piston by 1 wave still moves the solution to a different trough, but not to the bottom of the trough.

The phase shifting of the troughs that occurs in the asymmetric broadband case is due to two factors: frequency mismatch and spectrum asymmetry. Since the expected trough separation is in units of waves, the chosen reference wavelength is important. For an asymmetric broadband spectrum, we found that the mean wavelength or mean frequency may be a more appropriate reference wavelength than the center wavelength. For a symmetric broadband spectrum, the center wavelength and the mean wavelength are equal, which is why there is no
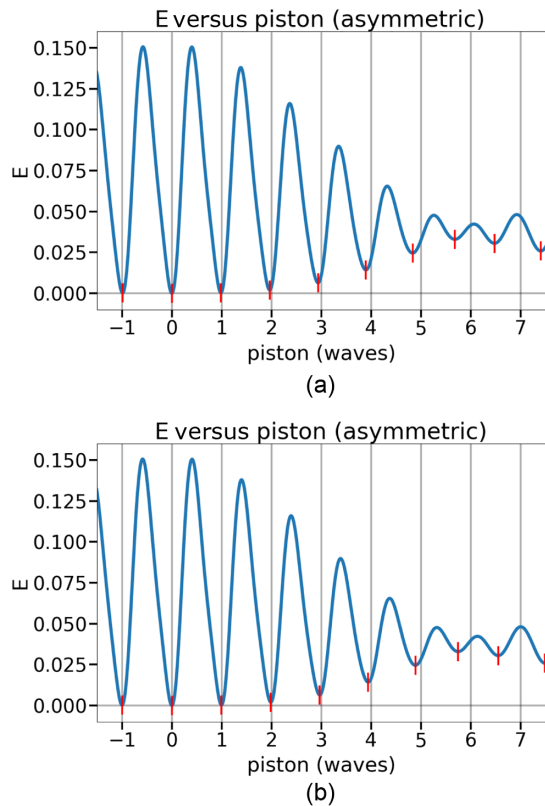
Fig. 4. (a) Zoomed in plot of Fig. 1(f), using the center wavelength of 18.06 µm as the reference wavelength. (b) Same as (a), but using the mean wavelength of 17.86 µm to account for frequency mismatch. Note that even after accounting for frequency mismatch, there are visible phase shifts at 5 and 6 waves—these are due to spectrum asymmetry.

frequency mismatch when using the center wavelength in that case. Figure 4(b) shows the trough locations of the same spectrum as in Fig. 4(a) but using the mean wavelength (17.86 µm in this case) as the reference wavelength rather than the center wavelength (18.06 µm). From Fig. 4(b) alone, it is tempting to say that we did not "frequency match" enough—perhaps an even smaller wavelength would be even better. However, using a smaller wavelength causes the trough error for negative waves (e.g., −6 to −1 waves) to get worse. Thus, we found that the mean wavelength gave a good compromise for both positive and negative troughs.

As seen in Fig. 4(b), even after accounting for frequency mismatch by using the mean wavelength, there are still visible phase shifts at 5 and 6 waves (in terms of mean wavelength). The remaining phase shift is due to spectrum asymmetry. This can be explained by the fact that the error metric value as a function of a single-segment piston is related to the real part of the temporal coherence function of the spectrum. This is further elaborated in Appendix A. The temporal coherence function is proportional to the Fourier transform of the spectrum. This is why for a symmetric broadband spectrum, the troughs are still 1 wave apart: the Fourier transform of a symmetric function has no phase component besides the linear term due to the center wavelength shift from the origin, so there is no phase-shifting of the troughs when taking the real part. However, the Fourier transform of an asymmetric broadband spectrum will have an additional phase component due to the asymmetry of

the spectrum, leading to phase shifting of the troughs when taking the real part. This is true within the coherence length of the spectrum—there may be other phase terms that lead to other phase shifts outside the coherence length even in the symmetric broadband case. For example, note in Fig. 1(d) that the troughs are at integers only out to 6 waves (the coherence length of the spectrum). After that, the bottoms of the troughs shift to half-integer values for a few waves. This is due to the negative sidelobes of the temporal coherence function (in this case, a sinc/Dirichlet function), which correspond to a phase shift of half a wave. This adds complexity to the grid search for larger values of the piston outside the coherence length for both broadband cases.

Even though in the asymmetric broadband case we are not at the bottom of the trough after changing the piston by 1 wave (in terms of center or mean wavelength), we can get to the bottom of the trough with a few steps of phase-retrieval optimization. Thus, our procedure differs from Paine's procedure by adding an optimization after performing the 2π piston phase jump in order to get to the bottom of each trough after each jump, as detailed in Section 5. Note that since what is important for the grid search is that changing the piston by 1 "wave" moves the solution to a different trough, our procedure can account for some frequency mismatch in addition to phase errors from spectrum asymmetry. This is beneficial because there are cases where the source spectrum is unknown, so obtaining an estimate of the mean wavelength may be difficult, but so long as the chosen reference wavelength, such as the center wavelength of the broadband filter, is close enough to the mean wavelength of the total spectrum, our procedure will still perform well. For this paper, we chose to use the center wavelength as our reference wavelength, but all of the principles still apply for any other reasonable reference wavelength.

4. SIMULATING A BROADBAND PSF

Since our work heavily depends on using broadband PSFs, we will now describe some of the nuances of simulating broadband PSFs.

We first take a closer look at the monochromatic PSF. Let the aperture amplitude transmittance array be $\boldsymbol{A}$, λ be the wavelength, and the pupil phase array at that wavelength be $\boldsymbol{\phi}$. The pupil sampling ratio is given by [6,7]

$$Q^{\mathrm{p}} = \frac{K}{M}, \tag{3}$$

where M is the number of samples across the pupil, and K is the padded array size for an FFT-based propagator. $Q^{\mathrm{p}} = 2$ corresponds to Nyquist sampling for the PSF [7]. The 2D discrete Fourier transform (DFT), assuming a square array, with a pupil sampling ratio of Q^{p}, is

$$G[r, s] = \mathscr{F}_{(Q^{\mathrm{p}})}\{g[m, n]\}$$

$$= \sum_{m,n} g[m, n] \exp\left\{-\mathrm{i}2\pi \frac{mr + ns}{K}\right\}$$

$$= \sum_{m,n} g[m, n] \exp\left\{-\mathrm{i}2\pi \frac{mr + ns}{Q^{\mathrm{p}} M}\right\}. \tag{4}$$

The PSF in the focus plane is computed as the squared magnitude of the Fourier transform of the aberrated pupil, which is then cropped to a region of interest. The PSF can be computed at a defocus plane, which can be done by adding a quadratic phase over the pupil. Thus, the monochromatic PSF can be expressed as

$$I_{\mathrm{mono}} = \boldsymbol{w}_{\mathrm{crop}} \circ \left| \mathscr{F}_{(Q^{\mathrm{P}})}\left\{ \boldsymbol{A} \circ \exp\left[\mathrm{i}2\pi\left(\frac{\boldsymbol{w}_p + \boldsymbol{w}_q}{\lambda} \right) \right] \right\} \right|^2,$$
(5)

where $\boldsymbol{w}_p$ is the pupil optical path error, $\boldsymbol{w}_q$ is the quadratic optical path error due to defocus, $\circ$ represents the Hadamard product, $\mathscr{F}_{(Q^{\mathrm{P}})}$ represents the Fourier transform with a pupil sampling ratio of Q^{P} as given by Eq. (4), and $\boldsymbol{w}_{\mathrm{crop}}$ represents the cropping operation, which can be thought of as multiplying by a binary mask. Note that $\boldsymbol{w}_p$ and $\boldsymbol{w}_q$ as well as λ are in units of length, making the exponent unitless. Thus, the pupil phase error is

$$\boldsymbol{\phi} = \frac{2\pi}{\lambda} \boldsymbol{w}_p,$$
(6)

and the defocus quadratic phase is

$$\boldsymbol{\theta} = \frac{2\pi}{\lambda} \boldsymbol{w}_q.$$
(7)

For a broadband PSF, we go from having a single wavelength to a spectrum with a non-zero bandwidth. We sample the spectrum at different, discrete wavelengths, λ_n, which have their corresponding spectral weights, S_n. A broadband PSF can be approximated as a sum of monochromatic PSFs, each weighted by S_n. However, special care must be taken to ensure that the monochromatic PSFs all have the same image sample spacing.

Here we model the pupil array to have the same sample spacing, Δx, for every wavelength, with M samples across the pupil, and let us assume a square array for simplicity. Then the DFT for a given Q^{P} will have an output spatial frequency sample spacing of

$$\Delta f_x = \frac{1}{K\Delta x} = \frac{1}{Q^{\mathrm{P}} M \Delta x}.$$
(8)

The image sample spacing, Δu, for an infinite-conjugate system (i.e., detection in the back focal plane of the lens) is related to Δf_x by

$$\Delta u = \lambda f \Delta f_x = \frac{\lambda f}{Q^{\mathrm{P}} M \Delta x},$$
(9)

where f is the focal length. Thus, for a given constant Q^{P}, Δu scales with λ. Because of this, for generating a broadband PSF, naively using the DFT with a fixed Q^{P} would cause each of the monochromatic PSFs to have different image sample spacings. However, the monochromatic PSFs should all have the same image sample spacing in order for the summation to be valid. Therefore, there should be a different Q_n^{P} for each λ_n.

Define λ_c as the central wavelength of the spectrum, and Q_c^{P} as the Q^{P} at λ_c. Then the PSF at λ_c will have some sample spacing Δu_c, and the Q_n^{P} are thus determined such that each individual monochromatic PSF at λ_n will also have a sample spacing of Δu_c:

$$Q_n^{\mathrm{P}} = \frac{\lambda_n}{\lambda_c} Q_c^{\mathrm{P}}.$$
(10)

Note that Q_n^{P} defined by Eq. (10) will likely have a non-integer padded array size. Thus, it may be useful to use alternative methods of computing the DFT that allow for arbitrary sampling, such as the matrix triple product or the chirp z-transform, instead of the FFT [7].

Therefore, a broadband PSF can be simulated as

$$I = \sum_n S_n \cdot \boldsymbol{w}_{\mathrm{crop}} \circ \left| \mathscr{F}_{(Q_n^{\mathrm{P}})}\left\{ \boldsymbol{A} \circ \exp\left[\mathrm{i}2\pi\left(\frac{\boldsymbol{w}_p + \boldsymbol{w}_q}{\lambda_n} \right) \right] \right\} \right|^2.$$
(11)

5. SEGMENT PISTON PHASE RETRIEVAL PROCEDURE

As an overview of the SPPR procedure, SPPR can be separated into two steps: global optimization and grid search. In the global optimization step, all of the segment pistons are optimized together until the solution is in a local minimum. In the grid search step, 2π piston phase jumps are applied to each segment and then the phase of that segment is optimized over, one segment at a time. Note that in the grid search step, optimization does occur, but only for one segment at any one time, as opposed to the global optimization step where all segments are optimized over simultaneously. After the first global optimization step, iterations of alternating grid search and global optimization steps are performed as needed. A reasonable stopping criterion is when the solution does not change after a grid search/global optimization iteration. However, as shown in Fig. 7 in Section 7 later, just having one grid search/global optimization iteration greatly increases the success rate of SPPR, with additional iterations providing diminishing returns. Note that the starting step and the final step are both global optimization steps. Every grid search step is followed by a global optimization step in order to settle the solution back down to a local minimum. If the final local minimum found is also the global minimum, then SPPR was successful; otherwise, the solution stagnated and SPPR failed. The capture range is thus defined as the set of starting points that converge to the global minimum. A flowchart of the SPPR procedure is shown in Fig. 5.

The optimizations that occur in both the global optimization and grid search steps are essentially traditional nonlinear-optimization phase retrieval. For optimization, the segment pistons are simulated on a segmented aperture, and then the corresponding broadband PSF according to the spectrum is computed as detailed in Section 2. The simulated PSF was compared to the measured/data PSF via an error metric, and then the gradient of the error metric with respect to the segment pistons was computed. The segment pistons are updated according to the gradients by the nonlinear optimizer, and then the process repeats until a local minimum of the error metric is found. During the global optimization step, all of the segments are optimized over simultaneously. On the other hand, during the grid search step, only one segment is optimized over at any one time, which occurs after applying an integer multiple of a 2π phase jump to that segment.

The grid search step is informed by our understanding of the error metric shape given in Section 3. A grid search step should
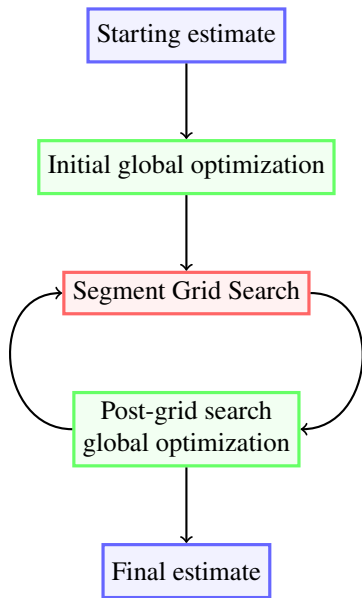
Starting estimate

↓

Initial global optimization

↓

Segment Grid Search

⟳

Post-grid search global optimization

↓

Final estimate

Fig. 5. Flowchart of SPPR procedure.

always be preceded by a global optimization step, so the initial solution for the grid search step will be at a local minimum of the error metric. First, we define the initial solution as the baseline solution, $\boldsymbol{\phi}_b$, with a corresponding baseline error metric value, E_b. Then, selecting a single segment at random, we apply an integer multiple of waves (in terms of center wavelength) of a piston to that segment in order to move the solution to a different trough, and then optimize over the piston of that segment to find the minimum error of that trough. We do this for a range of integer multiples of waves around the initial segment piston value in order to scan the troughs around $\boldsymbol{\phi}_b$. A parameter of the grid search step is what range to use. The scan limit is determined by the magnitude of expected segment piston error. In our case, that is determined by the previous alignment step. If the error metric value of the lowest trough is less than E_b, then we update $\boldsymbol{\phi}_b$ such that the piston of that segment is the piston value at the lowest trough, and E_b is also updated accordingly. We repeat this process for all segments, going through the segments one at a time randomly without repetition. We define going through all segments once as one round of grid searching. Each round of grid searching had a different random order of going through the segments. We continue doing rounds of grid searching until there is no improvement in E_b after an entire round. Going until there is no improvement after one round of grid searching is one grid search step in SPPR. The grid search step is very similar to what Paine did previously, but Paine did not perform an optimization after moving the solution to a different trough because Paine only examined symmetric broadband spectra [4].

6. SIMULATIONS

We used the WebbPSF Python package developed by Space Telescope Science Institute for an accurate model of MIRI's filters and object spectra [8]. We used a 5700 K blackbody for the object spectrum, and F1800W for the MIRI filter. We sampled the system spectrum with nine samples equally spaced in

wavelength across the bandwidth, as shown in Fig. 1(e), with a central wavelength, λ_c, of 18.06 μm.

For the aperture, we simulated a JWST-like aperture with a hexagonal two-ring configuration and a three-strut obscuration, as shown in Fig. 2. The pupil array was sampled with 512 pixels across five flat-to-flat hexagonal segment widths. The segments were simulated to be perfectly flat, i.e., the only error in the pupil is segment piston error. We used piston spread, defined as the peak-to-valley of the segment piston values, i.e., the maximum piston value minus the minimum piston value, in waves at λ_c to evaluate the magnitude of piston error. To account for the global piston, the segment piston errors were all relative to the same reference segment, in our case, the bottom segment of the inner ring.

For the broadband PSFs, we used a $Q_c^{\mathrm{P}} = 4$, using the flat-to-flat distance as the nominal diameter, to ensure that $Q_{\min}^{\mathrm{P}} > 2$, i.e., all individual monochromatic PSFs were oversampled along the maximum diameter (which is slightly longer than the flat-to-flat distance). We used the matrix triple product to compute the DFT and cropped the PSF array to the center 128-pixel square, and $\boldsymbol{w}_q$ was at 4 waves (at λ_c) peak to valley of defocus. For multiple trials, for the "measured" PSF, "true" segment piston errors were randomly generated with a uniform distribution and then scaled to have the correct amount of piston spread, and then 40,000 peak photons of Poisson noise and 12 photo-electrons (pe⁻) of Gaussian read noise were added to simulate measurement noise.

For optimizations, we used Thurman's bias-and-gain-invariant error metric [5], but we used the later formalization by Moore and Fienup [9]. We used L-BFGS [10] as the nonlinear optimizer, which requires gradient information that we computed via reverse-mode algorithmic differentiation as described by Jurling and Fienup [11]. Our initial estimate for the segment pistons was all zeros.

Using the coherence length as defined by Mandel and Wolf [12],

$$L_c = c\,\Delta\tau = c \int_0^\infty |\psi(\nu)|^2 \mathrm{d}\nu, \tag{12}$$

where $\psi(\nu)$ is the spectrum normalized to have unit area under the curve, the coherence length for the spectrum was approximately 6 waves (at λ_c). For the grid search steps, the first round of grid searching scanned up to ± 6 waves of the piston, and subsequent rounds scanned up to ± 12 waves of the piston.

For the full SPPR procedure used, we first performed a global optimization step, but we bound the segment piston values to be within one coherence length (± 6 waves at λ_c) from the reference segment. Then we removed the bound on the segment piston values and performed two iterations of a grid search step followed by a global optimization step. If, after any global optimization step, the error metric was below an error metric threshold of 1.5×10^{-4} (this value is explained in Section 7), then SPPR succeeded in finding the global minimum and we would stop the SPPR procedure early.

We performed the optimization process for integer piston spread values between 1 and 12 waves (at λ_c), inclusive. For each piston spread value, we examined 100 different cases of piston errors to obtain convergence statistics.
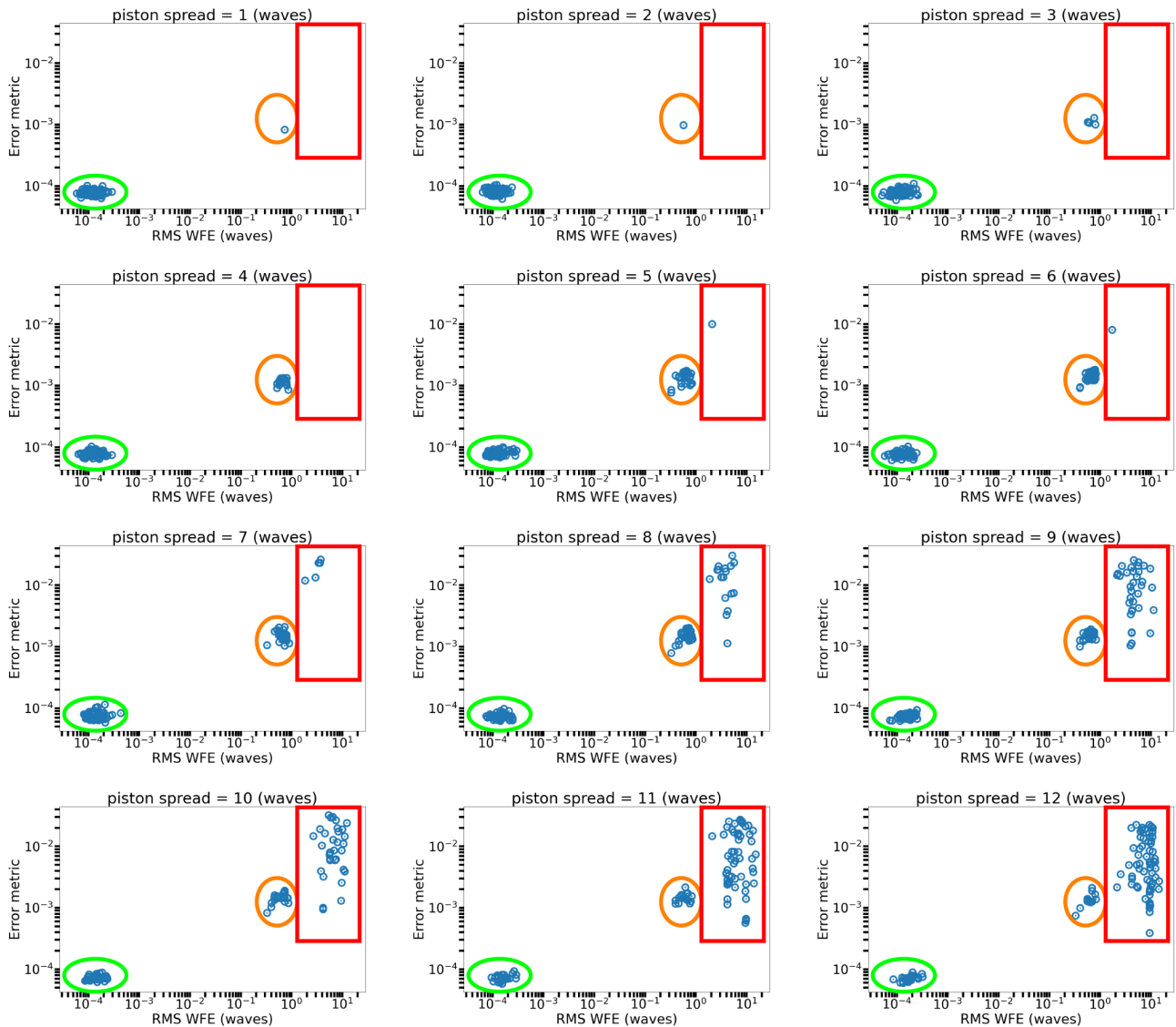
Fig. 6. Plots of final error metric value versus residual rms wfe for integer piston spread values between 1 and 12 waves (inclusive), 100 cases each. Piston spread increases across the row then down the column. Points encircled in green, encircled in orange, and boxed in red correspond to successful retrievals, split telescope failure mode, and runaway segments failure mode, respectively.

7. RESULTS

Figure 6 shows plots of the final error metric value versus the residual rms wavefront error (wfe) between the retrieved and true piston values for integer piston spread values between 1 and 12, inclusive, with 100 cases for each piston spread value. The cases can be separated into three groups. The points in the bottom left encircled in green correspond to successful retrievals, where SPPR found the true solution with high accuracy. The points encircled in orange and boxed in red correspond to two different failure modes. The points encircled in orange correspond to the split telescope failure mode, and the points boxed in red correspond to the runaway segment failure modes, which are the same failure modes encountered by Paine and Fienup [4]. Failure modes are discussed further in Section 8.

From Fig. 6, we determined that, for our simulations, a solution either converged to the true solution if the residual rms wfe was less than 10^{-3} waves rms (at λ_c), ended with the split telescope failure mode if the solution had a residual rms wfe between 10^{-1} and 1.3 waves rms (at λ_c), or ended with the runaway segments failure mode if the solution had a residual rms wfe greater than 1.3 waves rms (at λ_c). Using these criteria, we could easily categorize the different cases into the different groups. This is shown in Table 1, which shows the number of cases in each group for each plot in Fig. 6. However, in practice, we would only have access to the final error metric value. From Fig. 6, we determined that for our simulations, if the final error metric value was less than 1.5×10^{-4}, then the solution converged to the true solution and will have a residual wavefront error less than 0.4×10^{-3} waves rms at λ_c. Hence, by inspection of the error metric, we can with confidence say whether the SPPR ended in the global minimum (a success) or stagnated in a local minimum (a failure).

Figure 7 shows the SPPR success rate as a function of piston spread. The solid blue line shows the success rate if there

Table 1.   Breakdown of Cases Vs. Piston Spread[a]

Piston Spread (λ_c waves)	Successful	Split Telescope	Runaway Segments
1	99	1	0
2	99	1	0
3	95	5	0
4	84	16	0
5	71	28	1
6	68	31	1
7	61	34	5
8	51	32	17
9	43	23	34
10	46	21	33
11	27	17	56
12	23	12	65

[a]This is equivalent to the number of points inside the green, orange, and red regions in Fig. 6.
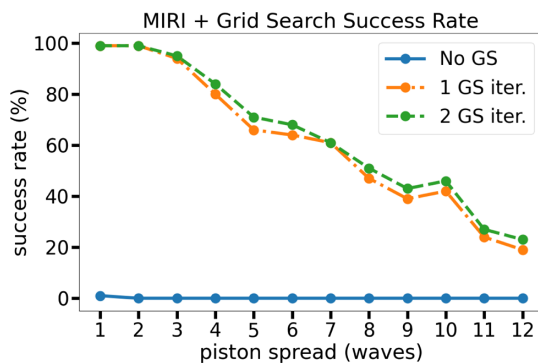
Fig. 7. Retrieval success rate versus piston spread. The solid blue line is after the initial global optimization step (no grid search), the dotted-dashed orange line is after one grid search and global optimization iteration, and the dashed green line is after two grid search and global optimization iterations. Note that the green line corresponds to the "successful" column in Table 1.

was no grid search. Out of 1,200 cases (12 piston spreads, 100 cases each), there was only one successful retrieval when the piston spread was 1 wave; the rest failed with no grid search. For a piston spread of 1, it is highly probable that one of the segment piston values will be greater than $\pm 1/2$ wave (in terms of λ_c) away from the reference segment, and that probability increases with increasing piston spread. Thus, the initial global optimization will most likely converge to the segment piston value that corresponds approximately to the true phase value modulo 2π. The dotted-dashed orange line shows the success rate with one grid search step. We can see that adding one grid search step greatly improved the success rate for lower piston spreads, and then the success rate steadily drops as piston spread increases. The dashed green line shows the success rate with two grid search steps. We see that adding the second grid search step did improve the success rate, but only marginally.

8. DISCUSSION

We showed that in simulation, assuming perfect segments having only piston errors, SPPR using MIRI's F1800W broadband filter and grid searching found the true solution up to

piston spreads of 216.7 µm (12 waves at 18.06 µm), and successful solutions had residual rms wavefront errors less than 7.2 nm (0.4×10^{-3} waves at 18.06 µm). The piston capture range of 216.7 µm was significantly larger than the ± 1.06 µm (half a wave at 2.12 µm) piston capture range of SPPR using NIRCam's F212N narrowband filter without grid searching, and the maximum residual rms wavefront error limit of 7.2 nm is less than the measurement requirement of 21.2 nm (10^{-2} waves at 2.12 µm). Thus, using MIRI's F1800W broadband filter and grid searching increased the capture range of SPPR over using NIRCam's F212N narrowband filter without grid searching while still meeting the measurement residual error requirement. Therefore, we demonstrated that a broadband long-wavelength channel can be used to significantly increase the capture range of SPPR. By increasing the capture range of SPPR, this relaxes requirements for how well previous alignment steps of coarse phasing need to align the segment pistons before using SPPR.

Our failure cases can be characterized into two failure modes: split telescope and runaway segments, both of which were observed by Paine and Fienup [4]. Examples of what the residual rms wfe of each failure mode may look like are shown in Fig. 8. These failure modes arise from the fact that we used a simplified grid search, where during the grid search we only moved one segment at a time. While a full grid search would avoid these failure modes, we found that a full grid search would be computationally infeasible.

The split telescope failure mode is characterized by a contiguous group of segments that are all in the same trough (i.e., same integer number of waves, typically ± 1) from the true solution. We can think of each segment as wanting to be in the same group as the majority of its nearest neighbors. The split telescope failure mode arises because correcting any one segment from the "incorrect" group either violates this majority rule, or is ambivalent (i.e., same number of segments in each group) and it settles on one or the other. Fixing this would involve including in the grid search moving contiguous groups of segments together, which has worse combinatorics and therefore is more computationally expensive as group size increases.

The runaway segments failure mode is characterized by individual segments (typically one) being very far (greater than one coherence length) away from the true solution. This may occur when the initial piston estimate for a segment is greater than a coherence length away from the true solution. In this case, during the grid search, the grid search may have the segment incorrectly go away from the true solution rather than towards it, and then it continues to walk further away until it eventually settles. A method to help fix this is to extend the grid search piston scan range, which increases the likelihood of finding the true solution trough at the cost of increased computational effort. When we increased the scan range from 6/12 waves to 12/18 waves for the first/subsequent rounds of the grid search, we found the success rate to increase by 5% from 23% to 28% for the piston spread of 12 waves case.

From Fig. 6, we can see that for piston spreads less than the coherence length of the spectrum (6 waves), the main failure mode was split telescope. Above the coherence length, the runaway segments failure mode becomes increasingly prevalent as piston spread increases. This makes sense because as the
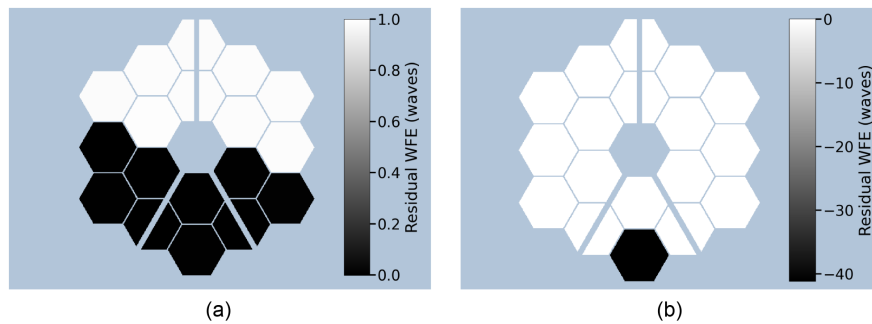
Fig. 8. Example residual wfe images demonstrating the two failure modes. Note the difference in scale of the colorbar. We added a background color to differentiate white segments on a white page. (a) Split telescope and (b) runaway segments.

piston spread increases above the coherence length, there is a higher likelihood that the initial segment piston estimate will be greater than one coherence length away from the true solution. Otherwise, for piston spreads below the coherence length, the main failure mode will be split telescope since split telescope may occur at any piston spread. We do see that split telescope cases also increase with increasing piston spread before runaway segments cases dominate.

We explored how far could we push the success rate beyond the 12 waves shown in Fig. 7. We found the success rate for piston spreads of 15, 20, and 25 waves, though we slightly modified the simulation procedure by allowing all grid search rounds to go up to ± the piston spread. The success rates at 15, 20, and 25 waves of piston spread were 7%, 2%, and 0%, respectively (i.e., at 25 waves, the success rate was <1%). Thus, the success rate steadily decreased to 0% at 25 waves, almost twice as far as what was shown in Fig. 7, as opposed to sharply dropping off beyond 12 waves.

In addition to the improvements to the grid search algorithm to deal with split telescope and runaway segments failure modes, higher success rates can also be achieved with multiple random starting guesses, since multiple random starting guesses (with appropriate piston spread) increase the probability of landing in the capture range. To test this, we looked at two cases of piston spread of 12 waves (at 18.06 μm) where it initially failed (one split telescope case and one runaway segments case), and we used 50 random starting guesses, where each random starting guess had a piston spread of 12 waves (at 18.06 μm). Out of the 50 random starting guesses, three guesses successfully converged in the split telescope case, and one guess successfully converged in the runaway segments case. Thus, while Fig. 7 shows the initial success rate of SPPR, multiple random starting guesses can help in cases that initially fail, thereby increasing the success rate. Therefore, the success rate can be significantly improved by performing SPPR with a modest number of random starting guesses and selecting the solution with the smallest final error metric value. The improvement of the success rate by increasing the number of random starting guesses comes at the cost of accordingly increased computation time, however. The number of random starting guesses needed for at least one to successfully converge increases as the initial success rate decreases, so the number of random starting guesses needed may be infeasible at very low initial success rates.

Even though we found that successful solutions of SPPR using MIRI's F1800W broadband filter and grid searching had residual rms wavefront errors of less than 7.2 nm (0.4×10^{-3} waves at 18.06 μm), which met our measurement requirement of 21.2 nm (10^{-2} waves at 2.12 μm), higher accuracy may be desired in other use cases. If higher accuracy is desired, our MIRI result can be used as a starting point for an SPPR using the NIRCam F212N narrowband filter and three defocus planes. We found that this additional optimization with NIRCam can improve accuracy by an additional factor of 10, which is related to the ratio of the central wavelengths of the MIRI F1800W filter (18.06 μm) and the NIRCam F212N filter (2.12 μm) and having multiple defocus planes.

Our main simulations only considered perfectly flat segments and no system aberrations, but we also did preliminary testing on how known intra-segment error and system aberrations would affect convergence percentage and accuracy. We performed another SPPR simulation, for a piston spread of 7 waves, where we applied JWST segment surface data to each segment as known intra-segment error, and we added MIRI system aberrations into the forward model as a known underlying wavefront error. The data for the JWST segment surface error and MIRI system aberrations were taken from WebbPSF, as shown in Fig. 9. We found the net rms wavefront error from intra-segment error and system aberrations to be approximately 0.069 μm, small enough that the system is still diffraction-limited even for NIRCam (Maréchal criterion of 1/14 waves rms at 2.12 μm for NIRCam is approximately 0.15 μm), which is accurate for the JWST. Figure 10 shows the plot of the final error metric value versus the residual rms wfe, analogous to the plots in Fig. 6, for this case with known intra-segment error and system aberrations. From Fig. 10, we can see that including known intra-segment error and system aberrations gives comparable convergence accuracy compared to our results with perfectly flat segments (less that 0.4×10^{-3} waves at 18.06 μm). Figure 11 shows the plot in Fig. 7 with the result from adding known intra-segment error and system aberrations included. From Fig. 11, we can see that including known intra-segment error and system aberrations did affect the convergence percentage, but not too much: with known intra-segment error and system aberrations, 53 out 100 cases converged after two grid search iterations, compared to 61 out 100 cases with perfectly flat segments, as shown in Table 1. While the initial success rate decreased after adding known intra-segment error and system aberrations, this
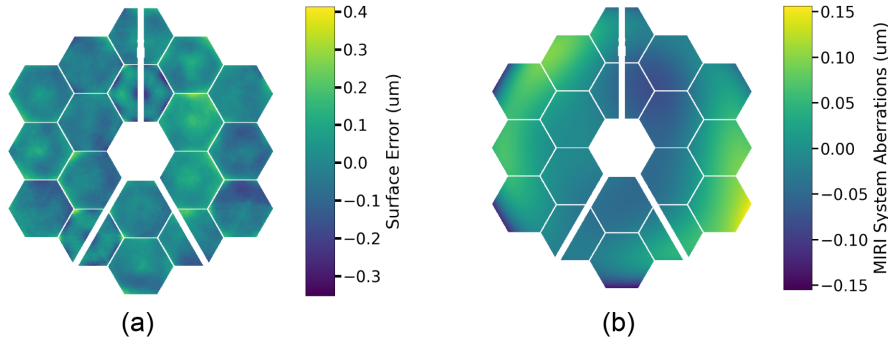
Fig. 9. (a) Intra-segment surface error taken from WebbPSF. Total rms wavefront error is approximately 0.067 μm. (b) MIRI system aberrations taken from WebbPSF. Total rms wavefront error is approximately 0.045 μm. Note difference in scale of the colorbars.
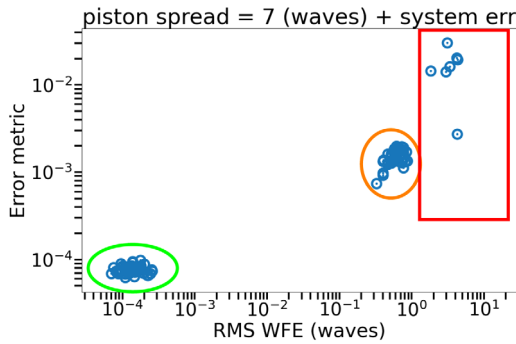

Fig. 10. Final error metric value versus residual rms wfe for 7 waves of piston spread with known intra-segment error and system aberrations (analogous to plots in Fig. 6).
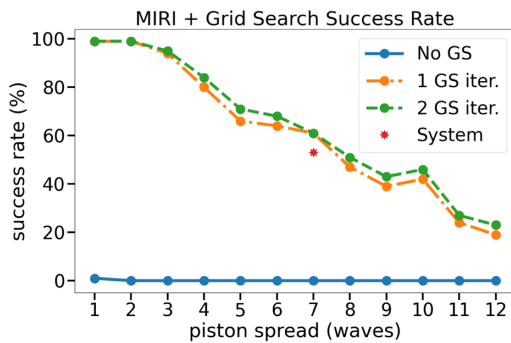

Fig. 11. Retrieval success rate versus piston spread plot from Fig. 7 with the result from known intra-segment error and system aberrations included. 53 out of 100 cases converged after two grid search iterations, compared to our result with no intra-segment error and no system aberrations, where 61 out of 100 cases converged (see Table 1).

could potentially be compensated for by adding a few multiple random starting guesses if the initial success rate is sufficiently high as mentioned previously. Thus, compared to our results with perfectly flat segments and no system aberrations, we found that while including known small intra-segment error and system aberrations did not affect convergence accuracy, it did affect convergence percentage somewhat.

In conclusion, segment piston phase retrieval with MIRI's F1800W broadband filter and grid searching was able to successfully find the true solution up to piston spreads of 217 μm

(12 waves at 18.06 μm) with a high success rate using a modest number of random starting guesses (≤ 50), and with final residual rms wavefront errors less than 7.2 nm (0.4×10^{-3} waves at 18.06 μm), though successful cases were still found up to 361 μm (20 waves at 18.06 μm). The capture range was increased many times over using NIRCam's F212N narrowband filter without grid searching, while maintaining the measurement requirement of residual rms wavefront error being less than 21 nm (10^{-2} waves at 2.12 μm). This greatly relaxes the requirements on the coarse phasing steps of commissioning the telescope. This may also be applied to the phasing up of multiple-telescope arrays.

APPENDIX A: CONNECTING ERROR METRIC AS A FUNCTION OF SINGLE-SEGMENT PISTON AND THE REAL PART OF THE TEMPORAL COHERENCE FUNCTION

We will now derive how the error metric varies as a function of the piston of a single segment.

Suppose we have a JWST-like aperture as shown in Fig. 2, and the only error is piston error of a single segment. Let us denote the segment with the error as A_n. Then the aberration-free aperture, A, can be separated into

$$A(x, y) = A_r(x, y) + A_n(x, y), \tag{A1}$$

where (x, y) are pupil coordinates, and A_r is the rest of the aperture without segment A_n.

Let p_n be the piston on segment A_n in units of microns, and $S(v)$ be the system spectrum as a function of frequency, v. Then the pupil field, g, is given by

$$g(x, y; p_n, v) = A_r(x, y) + A_n(x, y) \exp\left[i\frac{2\pi v}{c} p_n\right], \tag{A2}$$

where c is the speed of light. If $\mathscr{F}$ is the Fourier transform operator defined as

$$\mathscr{F}_{x \to f_x}\{g(x)\} = \int dx g(x) e^{-i2\pi x f_x} \tag{A3}$$

for the 1D case, then the image field, G, can be found as

$$G(\xi, \eta; p_n, \nu) = \mathscr{F}_{(x,y)\to(f_x, f_y)=\left(\frac{\xi\nu}{cf}, \frac{\eta\nu}{cf}\right)}\{g(x, y; p_n, \nu)\}$$

$$= \tilde{A}_r\left(\frac{\xi\nu}{cf}, \frac{\eta\nu}{cf}\right) + \tilde{A}_n\left(\frac{\xi\nu}{cf}, \frac{\eta\nu}{cf}\right)$$

$$\times \exp\left[i\frac{2\pi\nu}{c}p_n\right],$$

(A4)

where f is the system focal length. Note that $\tilde{A}_r$ and $\tilde{A}_n$ are in general both complex-valued.

The PSF at a single frequency is given by

$$I_\nu(\xi, \eta; p_n, \nu) = |G(\xi, \eta; p_n, \nu)|^2$$

$$= \left|\tilde{A}_r\left(\frac{\xi\nu}{cf}, \frac{\eta\nu}{cf}\right)\right|^2 + \left|\tilde{A}_n\left(\frac{\xi\nu}{cf}, \frac{\eta\nu}{cf}\right)\right|^2$$

$$+ \left\{\tilde{A}_r\left(\frac{\xi\nu}{cf}, \frac{\eta\nu}{cf}\right)\tilde{A}_n^*\left(\frac{\xi\nu}{cf}, \frac{\eta\nu}{cf}\right)\right.$$

$$\left.\times \exp\left[-i\frac{2\pi\nu}{c}p_n\right] + \text{c.c.}\right\}.$$

(A5)

The broadband PSF is thus given by

$$I(\xi, \eta; p_n) = \int_0^\infty d\nu\, S(\nu) I_\nu(\xi, \eta; p_n, \nu)$$

$$= I_1(\xi, \eta) + I_2(\xi, \eta; p_n),$$

(A6)

where

$$I_1(\xi, \eta) = \int_0^\infty d\nu\, S(\nu)\left(\left|\tilde{A}_r\left(\frac{\xi\nu}{cf}, \frac{\eta\nu}{cf}\right)\right|^2 + \left|\tilde{A}_n\left(\frac{\xi\nu}{cf}, \frac{\eta\nu}{cf}\right)\right|^2\right)$$

(A7)

and

$$I_2(\xi, \eta; p_n) = \int_0^\infty d\nu\, \tilde{A}_r\left(\frac{\xi\nu}{cf}, \frac{\eta\nu}{cf}\right)\tilde{A}_n^*\left(\frac{\xi\nu}{cf}, \frac{\eta\nu}{cf}\right) S(\nu)$$

$$\times \exp\left[-i\frac{2\pi\nu}{c}p_n\right] + \text{c.c.}$$

(A8)

$$= 2\text{Re}\left\{\mathscr{F}_{\nu\to\tau=\frac{p_n}{c}}\left\{\tilde{A}_r\left(\frac{\xi\nu}{cf}, \frac{\eta\nu}{cf}\right)\tilde{A}_n^*\left(\frac{\xi\nu}{cf}, \frac{\eta\nu}{cf}\right) S(\nu)\right\}\right\}.$$

(A9)

Note that only I_2 depends on p_n.

If the data PSF is given by the broadband PSF when $p_n = p_t$, where p_t is the true piston error value, and the PSF estimate is given by the broadband PSF when $p_n = p_e$, where p_e is the piston estimate, then the error metric as a function of p_e would be

$$E(p_e) = \iint d\xi\, d\eta\, [I(\xi, \eta; p_e) - I(\xi, \eta; p_t)]^2$$

$$= \iint d\xi\, d\eta\left[\int_0^\infty d\nu\, \tilde{A}_r\left(\frac{\xi\nu}{cf}, \frac{\eta\nu}{cf}\right)\tilde{A}_n^*\left(\frac{\xi\nu}{cf}, \frac{\eta\nu}{cf}\right) S(\nu)\right.$$

$$\left.\times \left(\exp\left[-i\frac{2\pi\nu}{c}p_e\right] - \exp\left[-i\frac{2\pi\nu}{c}p_t\right]\right) + \text{c.c.}\right]^2.$$

(A10)

$$= 4\iint d\xi\, d\eta\left[\text{Re}\left\{\mathscr{F}_{\nu\to\tau=\frac{p_e}{c}}\left\{\tilde{A}_r\left(\frac{\xi\nu}{cf}, \frac{\eta\nu}{cf}\right)\right.\right.\right.$$

$$\left.\left.\times \tilde{A}_n^*\left(\frac{\xi\nu}{cf}, \frac{\eta\nu}{cf}\right) S(\nu)\right\}\right\}$$

$$\left.- \text{Re}\left\{\mathscr{F}_{\nu\to\tau=\frac{p_t}{c}}\left\{\tilde{A}_r\left(\frac{\xi\nu}{cf}, \frac{\eta\nu}{cf}\right)\tilde{A}_n^*\left(\frac{\xi\nu}{cf}, \frac{\eta\nu}{cf}\right) S(\nu)\right\}\right\}\right]^2.$$

(A11)

From Eq. (A10), we see that the integral will be zero when the term in the parentheses that is the difference of two exponentials is zero, which occurs when

$$\frac{2\pi\nu}{c}p_e = \frac{2\pi\nu}{c}p_t + m2\pi$$

$$\Rightarrow p_e = p_t + m\lambda.$$

(A12)

Thus, for a monochromatic source, we should get a trough at every integer wave, which we see in Fig. 1(b). However, for a broadband spectrum, there is only perfect cancellation for all wavelengths at $m = 0$, or, conversely, for $m \neq 0$, there will be imperfect cancellation over all wavelengths, and thus there is only one null that occurs when $m = 0$. This is why the $m \neq 0$ troughs are not as deep as the $m = 0$ trough.

From Eq. (A11), recognizing that the temporal coherence function, $\gamma(\tau)$, is proportional to the Fourier transform of $S(\nu)$, we can see that the error metric is related to the real part of $\gamma(\tau)$. It would have been proportional to the real part of the $\gamma(\tau)$ had it not been for the additional $\tilde{A}_r\tilde{A}_n^*$ terms that are also functions of ν. This explains how the phase of $\gamma(\tau)$ is reflected in the error metric. The general trough spacing is due to the linear phase term in $\gamma(\tau)$ that comes from the center wavelength shift of $S(\nu)$ from the origin. However, the trough locations can be shifted around due to phases in $\gamma(\tau)$ that arise from the asymmetry of $S(\nu)$.

We want to reiterate that the error metric plots in Fig. 1 assume that the spectrum sampling is perfectly model-matched, and that the measured PSF is noiseless. When dealing with real data, the error metric plots will be less pristine.

Disclosures. The authors declare no conflicts of interest.

Data availability. Data underlying the results presented in this paper are not publicly available at this time but may be obtained from the authors upon reasonable request.

REFERENCES

1. D. S. Acton, J. S. Knight, A. Contos, _et al._, "Wavefront sensing and controls for the James Webb Space Telescope," Proc. SPIE **8442**, 84422H (2012).
2. M. D. Perrin, D. S. Acton, C.-P. Lajoie, _et al._, "Preparing for JWST wavefront sensing and control operations," Proc. SPIE **9904**, 99040F (2016).
3. J. R. Fienup, "Phase-retrieval algorithms for a complicated optical system," Appl. Opt. **32**, 1737–1746 (1993).

4. S. W. Paine and J. R. Fienup, "Extending capture range for piston retrieval in segmented systems," Appl. Opt. **56**, 9186–9192 (2017).

5. S. T. Thurman and J. R. Fienup, "Phase retrieval with signal bias," J. Opt. Soc. Am. A **26**, 1008–1014 (2009).

6. R. D. Fiete, "Image quality and $\lambda FN/p$ for remote sensing systems," Opt. Eng. **38**, 1229–1240 (1999).

7. A. S. Jurling, M. D. Bergkoetter, and J. R. Fienup, "Techniques for arbitrary sampling in two-dimensional Fourier transforms," J. Opt. Soc. Am. A **35**, 1784–1796 (2018).

8. STScI Telescopes Group, "WebbPSF simulation tool," Space Telescope Science Institute, 2022, https://www.stsci.edu/jwst/science-planning/proposal-planning-toolbox/psf-simulation-tool.

9. D. B. Moore and J. R. Fienup, "Ptychography for optical metrology with limited translation knowledge," Appl. Opt. **55**, 4596–4610 (2016).

10. D. C. Liu and J. Nocedal, "On the limited memory BFGS method for large scale optimization," Math. Program. **45**, 503–528 (1989).

11. A. S. Jurling and J. R. Fienup, "Applications of algorithmic differentiation to phase retrieval algorithms," J. Opt. Soc. Am. A **31**, 1348–1359 (2014).

12. L. Mandel and E. Wolf, "The measures of bandwidth and coherence time in optics," Proc. Phys. Soc. **80**, 894–897 (1962).